



Investigation of Mg^{2+} Ion Substitution on the Structural, Electric, and Magnetic Properties of Soft Spinel Ferrites ($NiFe_2O_4$) for High-Frequency Applications

Prachi Jain^{1,2} · S. Shankar² · O. P. Thakur¹

Received: 29 January 2024 / Accepted: 25 March 2024 / Published online: 28 April 2024
© The Minerals, Metals & Materials Society 2024

Abstract

Magnesium-doped nickel ferrite nanoparticles with the chemical composition ($Ni_{1-x}Mg_xFe_2O_4$, $x = 0.00, 0.20, \text{ and } 0.40$) have been prepared by a modified sol–gel citrate method. Structural analysis was carried out through x-ray diffractograms (XRD) and Fourier-transform infrared (FTIR) spectroscopy. The spherical-shaped morphology of the prepared nanoparticles has been confirmed by field-emission scanning electron microscopy (FESEM). The energy dispersive x-ray (EDX) analysis confirmed the presence of elements (Ni, Mg, Fe, and O) in the prepared compositions. The distribution of cations over tetrahedral and octahedral sites has been confirmed by Rietveld refinement using FullProf software. The phenomena of Maxwell–Wagner polarization is exhibited in the dielectric measurements. Cole–Cole plots showed that the net grain (R_g) and grain boundary resistance (R_{gb}) values are decreasing for the maximum concentration of Mg^{2+} ions in the nickel ferrites. Almost 96% deductions in the tangent loss values have been observed at high temperatures with the increasing concentration of Mg^{2+} ions in the nickel ferrites. Fitting of AC conductivity was carried out using the Jonscher Power Law function. The net magnetization saturation values also decreased from 27.7 emu/g to 16.7 emu/g upon the doping of Mg^{2+} ions in the pure nickel ferrites. These properties are all desired for materials working under high-frequency applications.

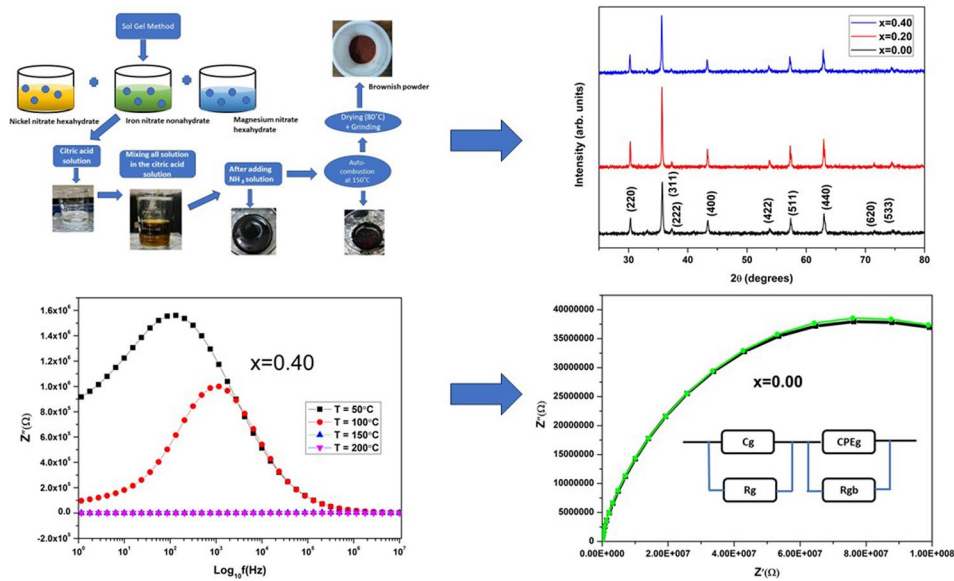
✉ S. Shankar
shankar3274@gmail.com; sssubramaniam@arsd.du.ac.in

✉ O. P. Thakur
ophthakur@nsut.ac.in

¹ Materials Analysis and Research Laboratory, Department of Physics, Netaji Subhas University of Technology, New Delhi 110078, India

² Functional Materials Research Laboratory, Department of Physics, ARSD College, University of Delhi, New Delhi 110021, India

Graphical Abstract



Keywords Ferrites · dielectric permittivity · rietveld refinement · dielectric loss · ferromagnetic

Introduction

Ferrites are well known for their excellent chemical stability and they cover a variety of applications in many fields, like biosensors, imaging, anti-fungal and anti-bacterial agents, humidity sensing, hydroelectric cells, supercapacitors, etc. Among all the ferrites, nickel ferrites are generally considered as a potential candidate that can show good electrical properties over other ferrites.¹ They can be utilized in fabricating transformer cores due to their high electrical resistivity. Nickel ferrites in the nanometer range exhibit a mixed spinel structure. Nickel ferrite nanoparticles have been proven to be beneficial in a variety of applications, like magnetic recording devices, electric generators, storage devices, etc., due to their high superparamagnetic behavior as well as high chemical stability.^{2,3} Exclusive research has been carried out on nickel ferrite nanomaterials due to their high magnetic permeability, low tangent loss, high saturation magnetization, high Curie temperature, and low coercivity.⁴ Extensive dielectric studies provide information regarding the conduction mechanism of ions inside the ferrites. A material's conductivity is subjected to various factors like sintering temperature, time, preparation condition, composition, cation distribution, etc.

Nickel ferrites lie in the group of soft spinel ferrites with the chemical formula $(M^{2+})(Fe^{3+})O_4^{2-}$, M occupies the octahedral lattice sites or B-sites while Fe ions occupy both the A and B interstitial lattice sites of the cubic lattice.⁵ The magnetic properties of nickel ferrites usually depend

upon the distribution of cations between the A or B sites. Magnesium ions have been chosen for doping into nickel ferrites due to their good electrical and magnetic properties.⁶ Magnesium is also considered non-toxic to the environment and has been utilized in various applications, like manufacturing mobile phones, laptops, storage devices, etc.⁷ Various synthesis methods are involved in the preparation Mg-doped NFO nanoparticles, like ball milling,⁸ co-precipitation,⁹ sol-gel,¹⁰ and hydrothermal.¹¹ Among these, the sol-gel method is generally preferred due to the low temperature, low cost, particle size in the nm range, high yield, and homogeneous morphology. Reddy et al. reported that a change in the calcined temperature caused an increase in particle size, magnetic saturation, and crystallinity.¹² Moradmard et al. found that doping of Mg²⁺ concentrations caused severe decreases in the saturation magnetization and a rise in coercivity (H_c).¹³ Here, different doping concentrations of Mg²⁺ ions have been performed on the nickel ferrites ($Ni_{1-x}Mg_xFe_2O_4$, $x = 0.00, 0.20, \text{ and } 0.40$). The structural, dielectric, and magnetic behavior of pure nickel ferrites have been observed and studied in detail.

Experimental

Magnesium-doped nickel ferrite nanoparticles ($Ni_{1-x}Mg_xFe_2O_4$, $x = 0.00, 0.20, \text{ and } 0.40$) for three different compositions were prepared using a sol-gel auto-combustion synthesis route. The step-by-step preparation

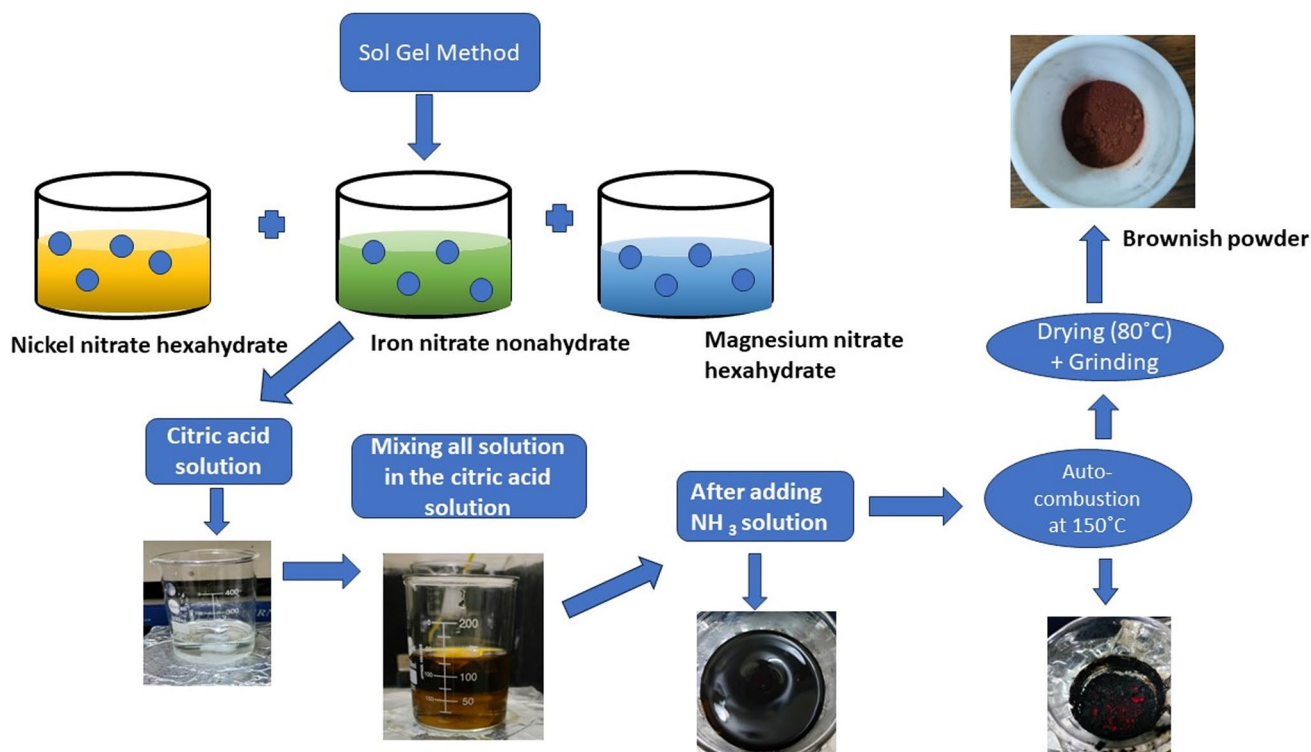


Fig. 1 Flowchart of Mg-substituted nickel ferrite nanoparticles via a sol-gel auto-combustion technique.

of Mg-substituted nickel ferrite nanoparticles is shown in Fig. 1. The stoichiometric amount of all the precursors ($\text{Ni}(\text{NO}_3)_2 \cdot 6\text{H}_2\text{O}$; 99%; Sigma Aldrich), ($\text{Fe}(\text{NO}_3)_3 \cdot 9\text{H}_2\text{O}$; 98%; Loba Chemie), and ($\text{Mg}(\text{NO}_3)_2 \cdot 6\text{H}_2\text{O}$; 98%; Loba Chemie) were dissolved in double-distilled water (DDW) using a magnetic stirrer at 300 rpm for 30 min each. Then, a 1-M citric acid solution was prepared separately by dissolving it in DDW. All the as-prepared nitrate solutions were poured gently into the citric acid solution. After 40 min of continuous mixing, the pH was balanced between 7 and 8 by adding NH_3 solution drop by drop into the final prepared solution. Then, the solution was constantly stirred at 300 rpm and heated to 80°C to form a viscous gel. After 10–12 h, a brown-colored sample powder was obtained. The powder was sintered at 800°C for 4 h to form the magnesium-substituted nickel ferrite nanoparticles. The weighed amounts of all the precursors required for the synthesis of each composition are set out in Table I.

Characterization

X-ray diffraction (XRD; D8 Advance; Bruker) measurements of the magnesium-doped nickel ferrites ($\text{Ni}_{1-x}\text{Mg}_x\text{Fe}_2\text{O}_4$ ($x = 0.00, 0.20$ and 0.40)) were carried out with Cu-K_α radiations ($\lambda = 1.5406 \text{ \AA}$) in the 2θ range extending from 20° to 80° with a scanning speed of $1^\circ/\text{min}$. Fourier-transform

Table I Precursor amounts of the prepared magnesium-doped nickel ferrites ($\text{Ni}_{1-x}\text{Mg}_x\text{Fe}_2\text{O}_4$)

Precursors	$x = 0.00$	$x = 0.20$	$x = 0.40$
$[\text{Ni}(\text{NO}_3)_2 \cdot 6\text{H}_2\text{O}]$	2.646	2.1306	1.6081
$[\text{Fe}(\text{NO}_3)_3 \cdot 9\text{H}_2\text{O}]$	7.353	7.3997	7.4466
$[\text{Mg}(\text{NO}_3)_2 \cdot 6\text{H}_2\text{O}]$	–	0.4696	0.9452

infrared (FTIR; Perkin Elmer) spectra were obtained for measurements in the range of $4100\text{--}400 \text{ cm}^{-1}$ for solid samples. The surface morphology of the samples was carried out using field-effect transmission electron spectroscopy–energy dispersive X-ray (FESEM-EDX; Zeiss). Dielectric, conductivity and the impedance measurements of all the samples were carried out by using a Nova Control Technology Impedance analyzer. Magnetic studies (M–H loop) were recorded using a vibrating sample magnetometer (VSM; ADE-EV9) under a magnetic field of 1 tesla obtained at room temperature.

Results and Discussions

XRD Analysis

The XRD pattern of the Mg-doped nickel ferrites has been obtained at room temperature in the 2θ range varying from

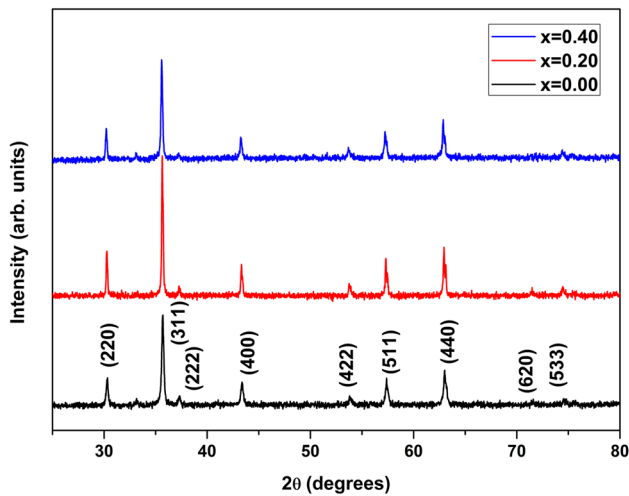


Fig. 2 X-ray diffraction pattern of Mg-doped nickel ferrites ($\text{Ni}_{1-x}\text{Mg}_x\text{Fe}_2\text{O}_4$ ($x = 0.00, 0.20$ and 0.40)).

Table II Essential parameters obtained through the Rietveld refinement for Mg-doped nickel ferrites ($\text{Ni}_{1-x}\text{Mg}_x\text{Fe}_2\text{O}_4$, $x = 0.00, 0.20$ and 0.40)

Parameters	$x = 0.00$	$x = 0.02$	$x = 0.04$
Crystallite size (nm)	27.889	39.212	36.313
Microstrain ($\epsilon \times 10^{-3}$)	2.17	1.83	1.52
χ^2	1.51	1.30	1.02
Lattice parameter ($a = b = c$) (Å)	8.338	8.3416	8.350
Volume (Å ³)	579.709	580.427	582.323
X-ray density (g/cm ³)	6.630	6.671	6.493
Bulk density (g/cm ³)	3.057	2.802	2.547
Porosity (%)	53.880	57.989	60.761

20 to 80°, as shown in Fig. 2. The peak positions have been correctly matched with the JCPDS card No. #10-325.¹⁴ The prepared ferrite comes under the category of cubic spinel ferrite with the $Fd-3m$ space group. The highly intensified peak occurring in the (311) plane indicates the presence of a single face-centered cubic spinel structure, whereas the impurity peak present at 32° corresponds to the Fe_2O_3 phase.¹⁵

The shifting of the peaks towards the right side has been observed upon the doping of Mg^{2+} ions in nickel ferrites. The average crystallite size of the Mg-doped nickel ferrites has been calculated using the Debye–Scherrer equation¹⁶:

$$D = \frac{0.9\lambda}{\beta \cos\theta} \quad (1)$$

where D is the crystallite size, λ is the wavelength of x-ray radiation (0.154 nm), β is the full width at half-maximum (FWHM) of the peaks, and θ is the diffraction angle.

All the essential parameters, like crystallite size, porosity%, x-ray density, bulk density, microstrain, lattice parameter, volume, etc., are set out in Table II. Experimental values of the lattice parameter, x-ray density, bulk density, and porosity (%) have been calculated using Eqs. (2)–(5):

$$\text{Lattice parameter} = d\sqrt{h^2 + k^2 + l^2} \quad (2)$$

$$\text{X-ray density}(D_x) = \frac{8M}{Na^3} \quad (3)$$

$$\text{Bulk density}(D_b) = \text{Mass of pellet}/\text{Volume of pellet} = m/\Pi r^2 L \quad (4)$$

$$\text{Porosity}(\%) = 1 - D_b/D_x \quad (5)$$

Williamson–Hall Plots

Williamson–Hall (W–H) plots usually establish the relationship between strain and crystallite size.¹⁷ The W–H plot equation is:

$$\beta \cos\theta = (4\sin\theta)\epsilon + \frac{K\lambda}{D} \quad (6)$$

where ϵ is the lattice strain developed owing to the imperfections in the cubic lattice of nickel ferrite, β is the FWHM, and D represents the average crystallite size for each composition.

The slope obtained from the W–H plots in Fig. 3 provides the value of (FWHM)microstrain produced in the samples. The average crystallite size has been calculated using the intercept of the W–H plot equation. It has been observed that the porosity% is increasing with the rise in the doping% of magnesium ions in the nickel ferrites. This is mainly due to the difference in the ionic radii of ions present in the sample. Generally, the ionic radii of Mg^{2+} (0.72 Å) ions is greater than the ionic radii of the Ni^{2+} (0.69 Å) and Fe^{3+} (0.645 Å) ions. The difference in the sizes induce some strain in the samples and gives rise to the increased value of the lattice constant.

Rietveld Refinement Analysis

The Rietveld refined graphs for the XRD patterns of all the prepared samples have been carried out using the FullProf software, as shown in Fig. 4. The refinement has been performed by assuming a cubic structure where $a = b = c$ and $\alpha = \beta = \gamma = 90^\circ$. The refinement has been brought up by refining the global parameters, such as background and scale factors, followed by the refinement of the lattice constants,

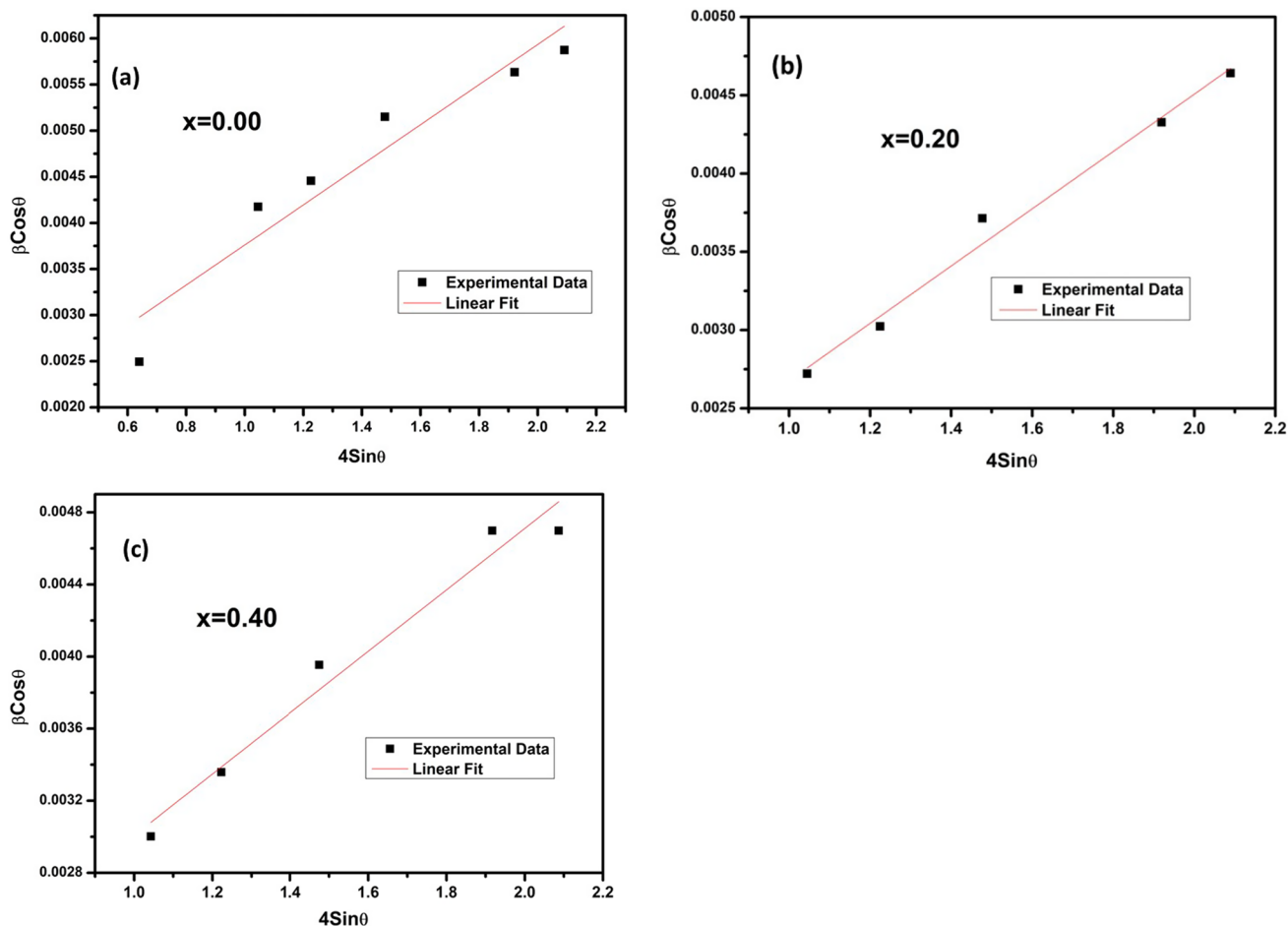
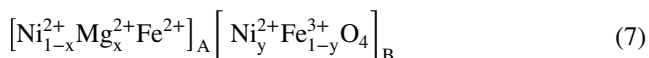


Fig. 3 Williamson–Hall plots of the magnesium-doped nickel ferrites, $\text{Ni}_{1-x}\text{Mg}_x\text{Fe}_2\text{O}_4$: (a) $x = 0.00$, (b) $x = 0.20$, and (c) $x = 0.40$.

crystal symmetry, shape parameters, background correction, metal ion occupancies, atom positions, and thermally varying parameters. The refinement has been carried out by selecting the profile as the Thomson–Cox pseudo-Voigt. Figure 4 shows the refined XRD profile, where the black one shows the experimental data, the red one exhibit the Rietveld fitted curve, the green one the Bragg positions, and the blue one the difference in the experimental and fitted intensities.¹⁸ It has been observed that Mg^{2+} ions occupy the tetrahedral site or A sites due to their smaller ionic radii compared to the nickel ion (0.7 Å). However, nickel and iron ions are equally distributed among both the A and B sites.¹⁹ The cationic distribution among the A and B sites are represented by Eq. (8), below. The distribution of cations (Mg^{2+} , Fe^{2+} or Fe^{3+} , Ni^{2+}) among the tetrahedral and octahedral sites is shown in Table III, obtained using Rietveld refinement. The general formula for the allocation of cations at the A and B sites is:



The spinel ferrite has a cubic close-packed structure with large amount of O^{2-} ions present at the corners of the lattice. A total number of 32 octahedral as well as 64 tetrahedral lattice sites are present in the cubic lattice of spinel ferrites, of which divalent ions occupy 8 tetrahedral sites while 16 octahedral sites are made available for trivalent ions.

FT IR Analysis

FTIR is used to determine the effective bonds present in the material or in any spinel ferrite. Formation of the bonds present in the magnesium-substituted nickel ferrite can be confirmed by studying the FTIR spectra, as shown in Fig. 5. Spinel ferrites exhibit mainly two absorption bands within the range of $400\text{--}650\text{ cm}^{-1}$.²⁰ The first band occurs at 400 cm^{-1} due to the stretching vibration of metal–oxygen ions at octahedral sites while the second band comes at 547 cm^{-1} corresponding to the stretching vibration at tetrahedral sites.²¹ The peak around the wavenumber 1358 cm^{-1} is due to the bending vibration of O–H bonds, and that at 1600 cm^{-1} to the bending mode of the H_2O molecule.

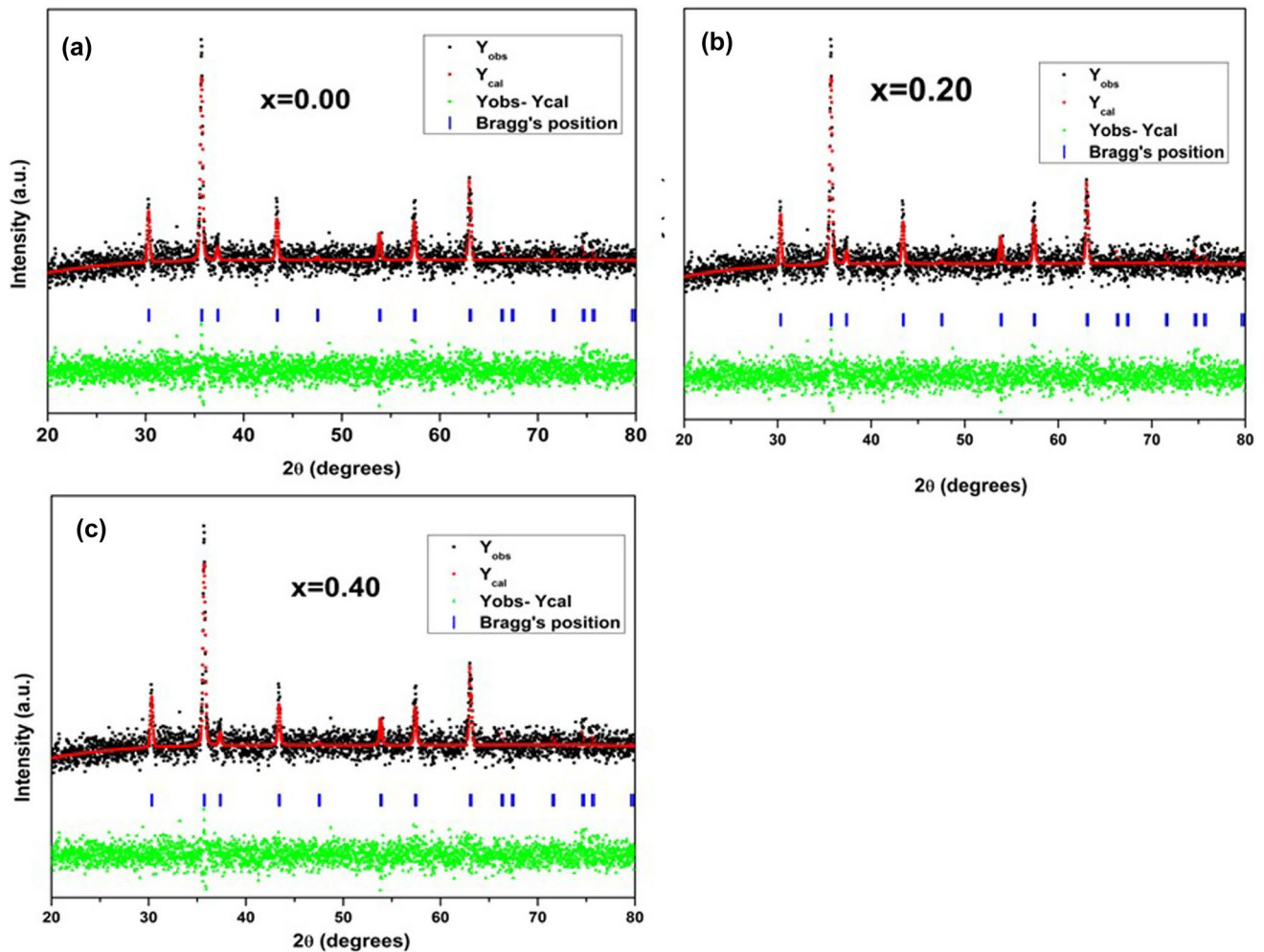


Fig. 4 Rietveld refinement of the Mg substituted nickel ferrites, $\text{Ni}_{1-x}\text{Mg}_x\text{Fe}_2\text{O}_4$: (a) $x = 0.00$, (b) $x = 0.20$, and (c) $x = 0.40$ using FullProf software.

Table III Cation distribution among the A sites and B sites, as obtained through Rietveld refinement plots

Composition	A-site	B-site
$x = 0.00$	$(\text{Ni}_{0.08}\text{Fe}_{0.90})_A$	$(\text{Ni}_{0.92}\text{Fe}_{1.10})_B$
$x = 0.20$	$(\text{Ni}_{0.05}\text{Fe}_{0.95})_A$	$(\text{Ni}_{0.75}\text{Mg}_{0.20}\text{Fe}_{1.05})_B$
$x = 0.40$	$(\text{Ni}_{0.02}\text{Fe}_{0.98})_A$	$(\text{Ni}_{0.58}\text{Mg}_{0.40}\text{Fe}_{1.02})_B$

Morphological Analysis

FESEM is a highly resolved technique in which the scanning of a sample surface is carried out using a highly intense sharp beam of electrons to understand the composition of elements present in the sample. Figure 6 shows the FESEM images of the samples along with their size distribution curves. The particle size varied from 37 to 69 nm, which was calculated using ImageJ software. It has been noticed that the porosity in the samples has been increased on adding

Mg ions to the nickel ferrite. The FESEM images show the spherical-shaped nanoparticles, and the uniformity in the prepared samples increases with the increase in Mg ions.²² Figure 7 shows the EDX spectra of the Mg-doped nickel ferrites and Table IV presents the atomic as well as weight% of all the elements present in the composition.

Dielectric Measurements

The variation of real values of dielectric permittivity (ϵ') with frequency (1 Hz–10 MHz) for all the samples (Mg-doped nickel ferrite) at different values of temperature (50°C, 100°C, 150°C, and 200°C) is shown in Fig. 8(a–c). It has been observed that ϵ' decreases very rapidly as the frequency increases from a few Hz to a few MHz. In this frequency range, dipolar and interfacial polarizations are more active. In the low-frequency regime, ϵ' has very high values while at high frequency, the ϵ' becomes very low or almost minimum. This fall of ϵ' is due to the inability of dipoles to

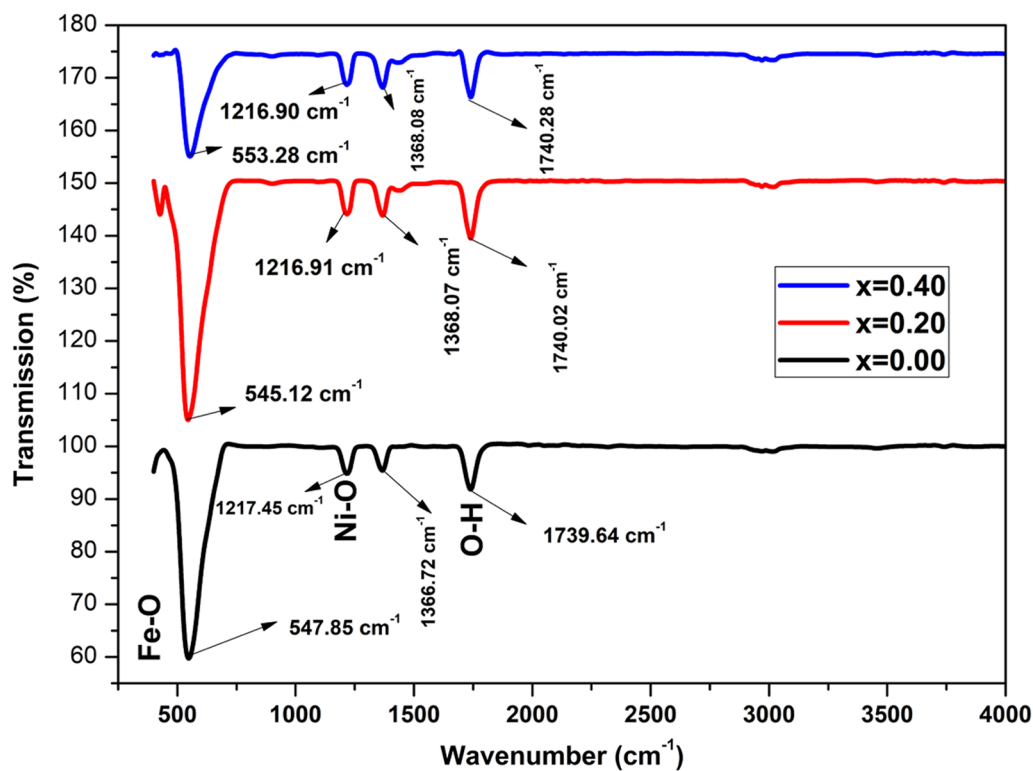


Fig. 5 FTIR spectra of Mg-doped nickel ferrites, $\text{Ni}_{1-x}\text{Mg}_x\text{Fe}_2\text{O}_4$, $0 \leq x \leq 0.40$.

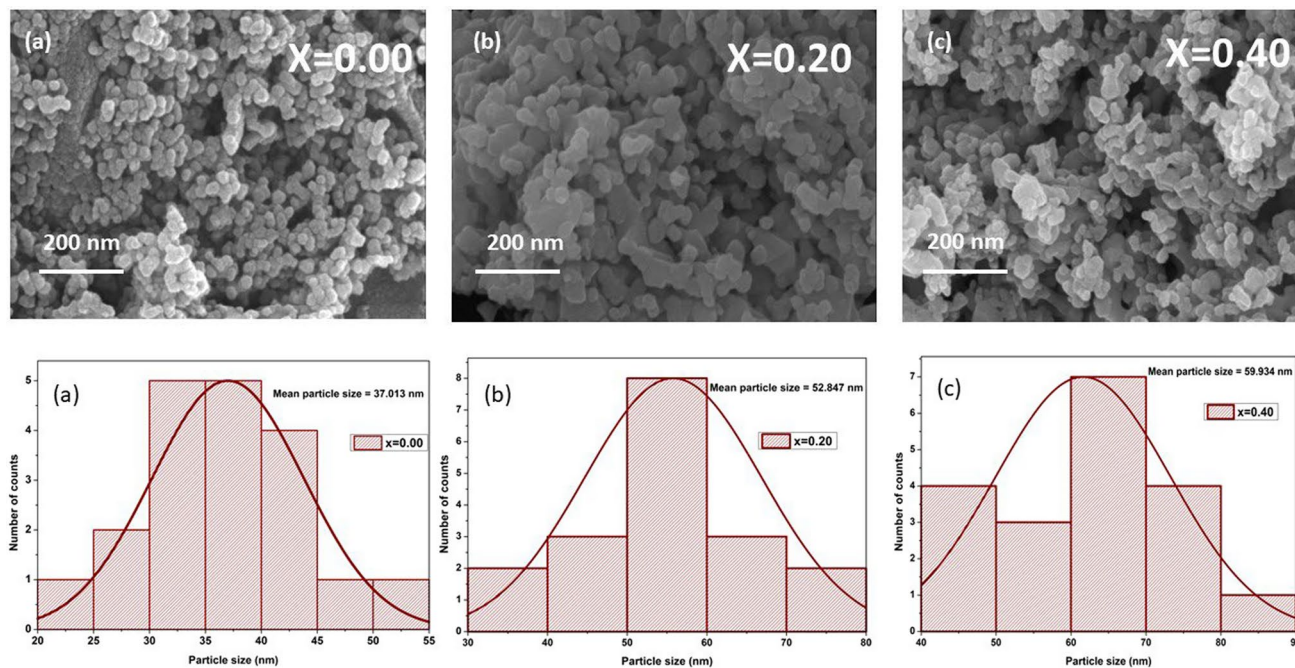


Fig. 6 Field-emission scanning electron microscopy images and size distribution curves for Mg-doped nickel ferrites, $\text{Ni}_{1-x}\text{Mg}_x\text{Fe}_2\text{O}_4$: (a) $x = 0.00$, (b) $x = 0.20$, and (c) $x = 0.40$.

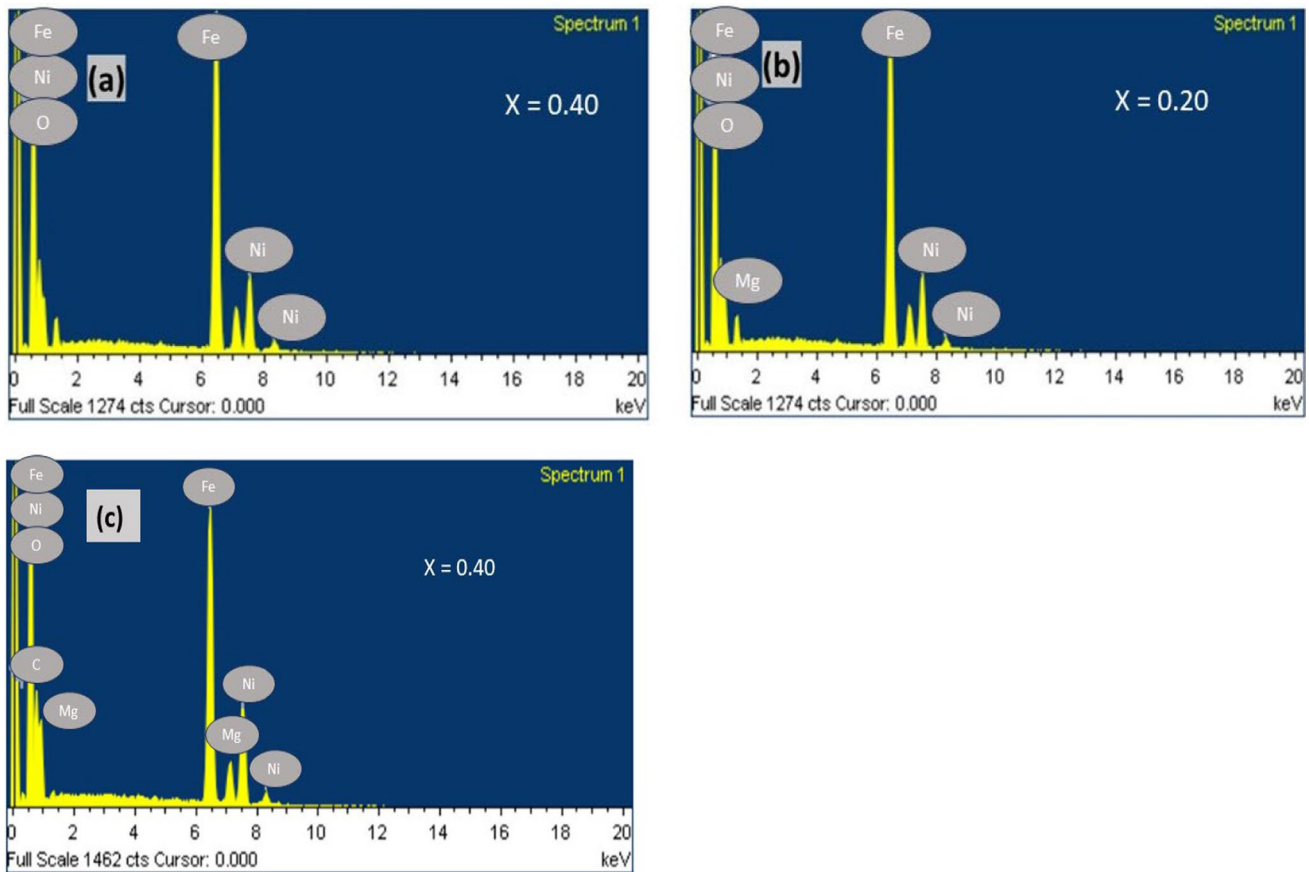


Fig. 7 EDX spectra of the Mg-doped nickel ferrites, Ni_{1-x}Mg_xFe₂O₄: (a) $x = 0.00$, (b) $x = 0.20$, and (c) $x = 0.40$.

Table IV EDX results for Mg-doped nickel ferrites nanoparticles sintered at 800°C

Elements	NiFe ₂ O ₄ ($x = 0.00$)		Ni _{0.8} Mg _{0.2} Fe ₂ O ₄ ($x = 0.20$)		Ni _{0.6} Mg _{0.4} Fe ₂ O ₄ ($x = 0.40$)	
	Atomic (%)	Weight (%)	Atomic (%)	Weight (%)	Atomic (%)	Weight (%)
Ni	9.10	19.10	6.32	15.25	5.64	10.90
Fe	20.28	40.50	24.56	46.70	28.86	53.06
O	70.62	40.40	61.24	35.53	59.61	40.14
Mg	–	–	5.89	2.12	7.88	4.10

align themselves along the direction of the changing electric field.²³ This dispersion of the dielectric constant shows the space charge polarization and notifies the Maxwell–Wagner polarization.²⁴ For the temperature of 50°C and frequency of 100 Hz, the value of ϵ' is reduced from 2000 to 102 on incorporating Mg²⁺ ions in the nickel ferrite. The dispersion in the ϵ' is mainly due to the electron hopping between the Fe²⁺ \leftrightarrow Fe³⁺ ions and the value of ϵ' given by:

$$\epsilon_r = \epsilon_{r\infty} + \frac{\epsilon_r - \epsilon_{\infty}}{1 + (\omega\tau)^{1-\alpha}} \quad (8)$$

It can be seen from Fig. 8 that, on increasing the temperature values, the ϵ' value also increases in each composition,

indicating the diffusive type relaxor behavior in the prepared ferrites.²⁵

In the pure nickel ferrites, Ni²⁺ ions and half of Fe³⁺ ions are occupied in the octahedral sites or B sites, while half of the Fe²⁺ ions are occupied in the tetrahedral lattice sites. Ni²⁺ and Ni³⁺ ions both constitute p -type charge carriers, while Fe²⁺ and Fe³⁺ ions lead to n -type charge carriers or electrons. Electrons are the only charge carriers at the tetrahedral sites due to the presence of Fe²⁺ ions.²⁶ The rise in the concentration of Fe²⁺ ions gives rise in the high value of the dielectric constant. A major contribution in the ϵ' value is due to the Fe²⁺ ions which are present only at the tetrahedral sites because Fe²⁺ ions

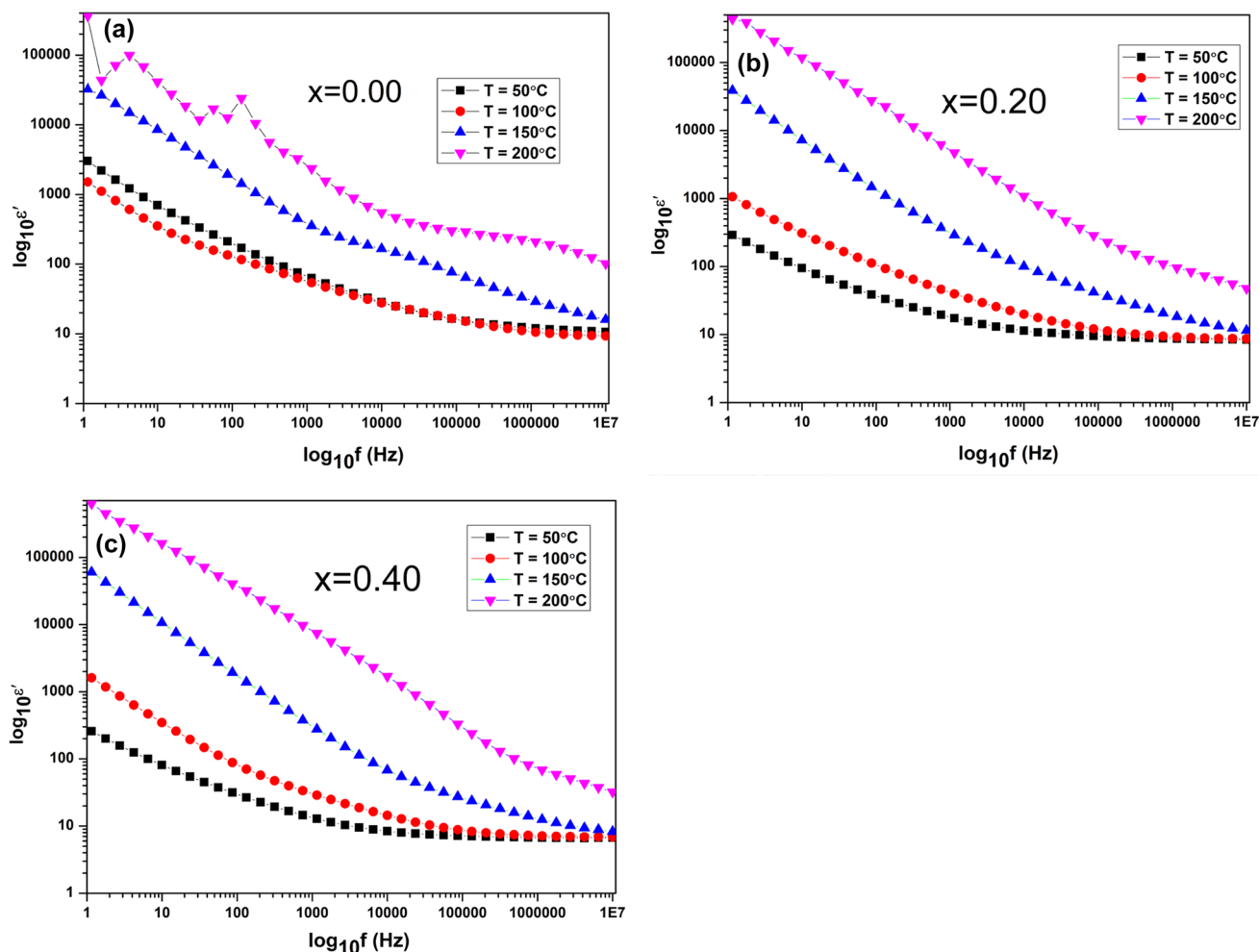


Fig. 8 Variation of dielectric constant (ϵ') with frequency for the (a) NiFe_2O_4 , (b) $\text{Ni}_{0.8}\text{Mg}_{0.2}\text{Fe}_2\text{O}_4$, and (c) $\text{Ni}_{0.6}\text{Mg}_{0.4}\text{Fe}_2\text{O}_4$.

become more easily polarized than the Fe^{3+} ions. Now, substituting Mg^{2+} ions in nickel ferrite causes the movement of a small amount of Fe^{2+} from its tetrahedral sites to octahedral sites. In other words, adding Mg^{2+} ions cause a disturbance in the dipole alignment of the Fe^{2+} ions, which will cause a reduction in the ϵ' values. Basically, the presence of Mg^{2+} ions leads to a rise in p -type charge carriers and Fe^{2+} gives rise to n -type charge carriers, which may be due to the electron exchange between Fe^{2+} and Fe^{3+} ions.

For $x = 0.00$ and 0.40 , there is a change in slope or rapid decrement in the values of the dielectric constant occurring at $T = 200^\circ\text{C}$. This has occurred because, at high temperatures, the thermal activation phenomenon takes place. According to this phenomenon, the molecular motion is vigorously rising inside the material. The increased motion of the molecules leads to disruption in the alignment of the dipoles and, thereby, causes a reduction in the value of ϵ' .

Tangent Loss

The plot of dielectric loss against frequency ranging from 1 Hz to 10 MHz at different values of fixed temperature (50°C , 100°C , 150°C , and 200°C) for the prepared samples is shown in Fig. 9a, b, and c. Figure 9d represents the comparison of the losses present in all the prepared samples at $T = 50^\circ\text{C}$. Figure 9a, b, and c concludes that, at low frequency values, the loss value decreases from 10.26 to nearly 1 with increasing the Mg content in the nickel ferrites. This is generally due to the increase in the crystallinity over the increase in Mg content in the nickel ferrites. The temperature dependence of loss exhibits the occurrence of peaks at high-temperature values, attributed to the presence of relaxation phenomena in the prepared ferrites.²⁷ The samples show high losses at higher temperatures. This high tangent loss means the possibility of the conversion of electrical energy into heat in the form of various applications.

For $x = 0.00$, in the low-frequency region, bound charges, such as polarization charges connected to polar

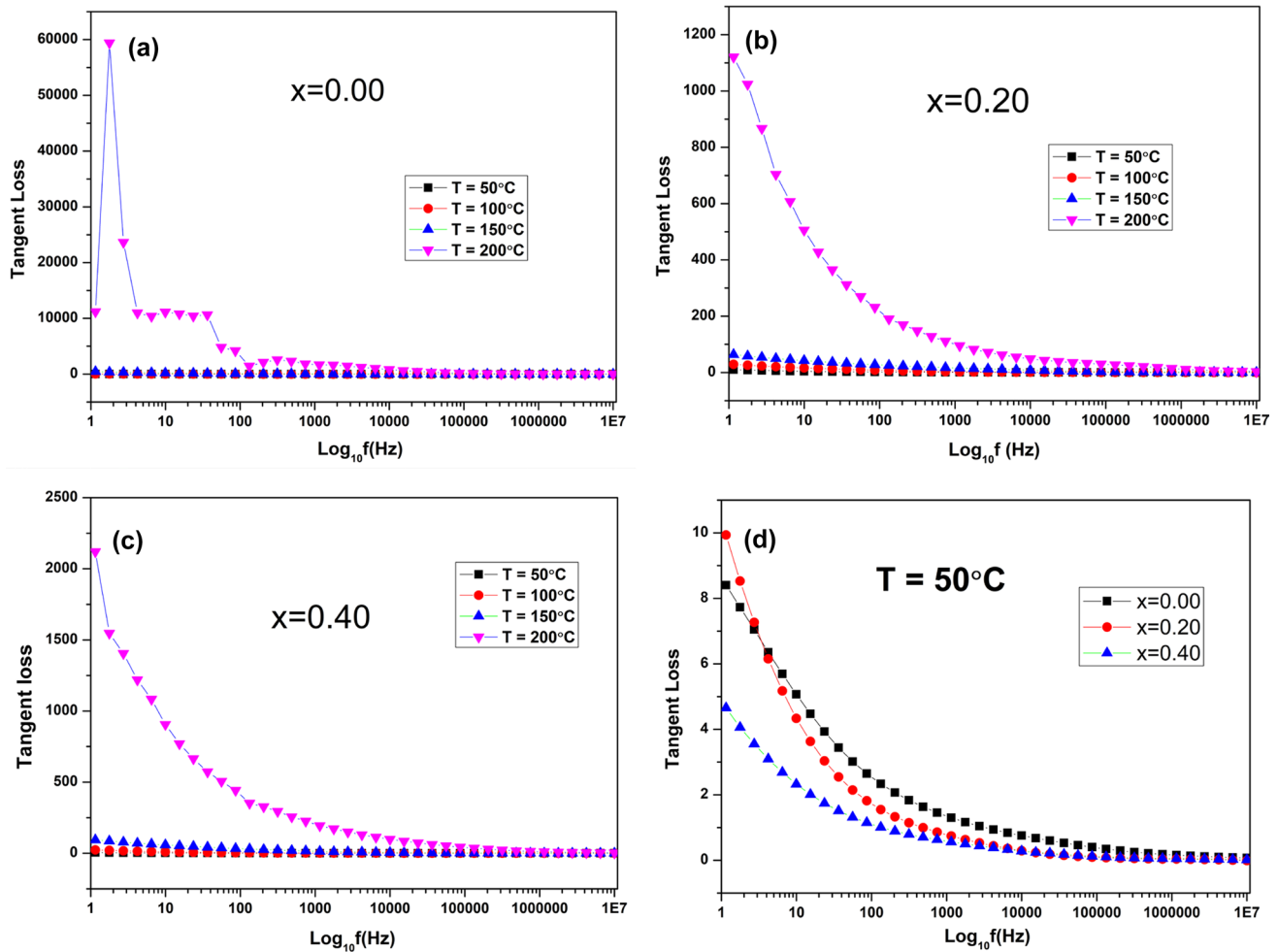


Fig. 9 Tangent loss against frequency at different temperatures (50°C, 100°C, 150°C, and 200°C) for Ni_{1-x}Mg_xFe₂O₄: (a) 0.00, (b) 0.20, (c) 0.40, and (d) comparison of tangent loss plots at room temperature.

molecules or ions, are frequently present in dielectric materials. These bound charges might have enough time at low frequencies to react to the applied electric field, which would cause a large amount of energy dissipation and an increase in the loss tangent. The strong ionic or dipolar interactions in the materials cause this effect to be especially noticeable.

Variation of Z'' with Frequency at Different Temperature Values

The variation in the Z'' against $\log_{10}f$ with frequency values ranging from 1 Hz to 10 MHz has been recorded for the Mg-doped nickel ferrite samples, as shown in Fig. 10a, b, and c. The Z'' peak diminishes as the temperature value increases from the lowest to the highest values, representing the lossy nature of the ferrites.²⁸ Also, the Z'' peak is shifted to a higher frequency or towards the right side for higher temperature regimes, validating the occurrence of non-Debye-type diffusive relaxation mechanism in the Mg-doped nickel ferrites.²⁹ The Z'' peak becomes broadened

for higher temperature values, showing the existence of a thermally activated relaxation process. This shifting of the peaks towards higher frequency values is due to the movement of immobile species or defects at high temperature. It is beneficial to study fast switching-based device applications under an applied electric field.

Impedance Measurements

The Nyquist plots or Cole–Cole plots of the Mg-doped nickel ferrites at different temperatures are shown in Fig. 11a, b and c. The effective contributions from the grains as well as the grain boundaries are given by:

$$Z^* = \frac{R_1}{1 + i\omega R_1 C_1} + \frac{R_2}{1 + i\omega R_2 C_2} \quad (9)$$

In all the samples, only a single arc occurs, which confirms the conductivity due to the presence of just grains.³⁰

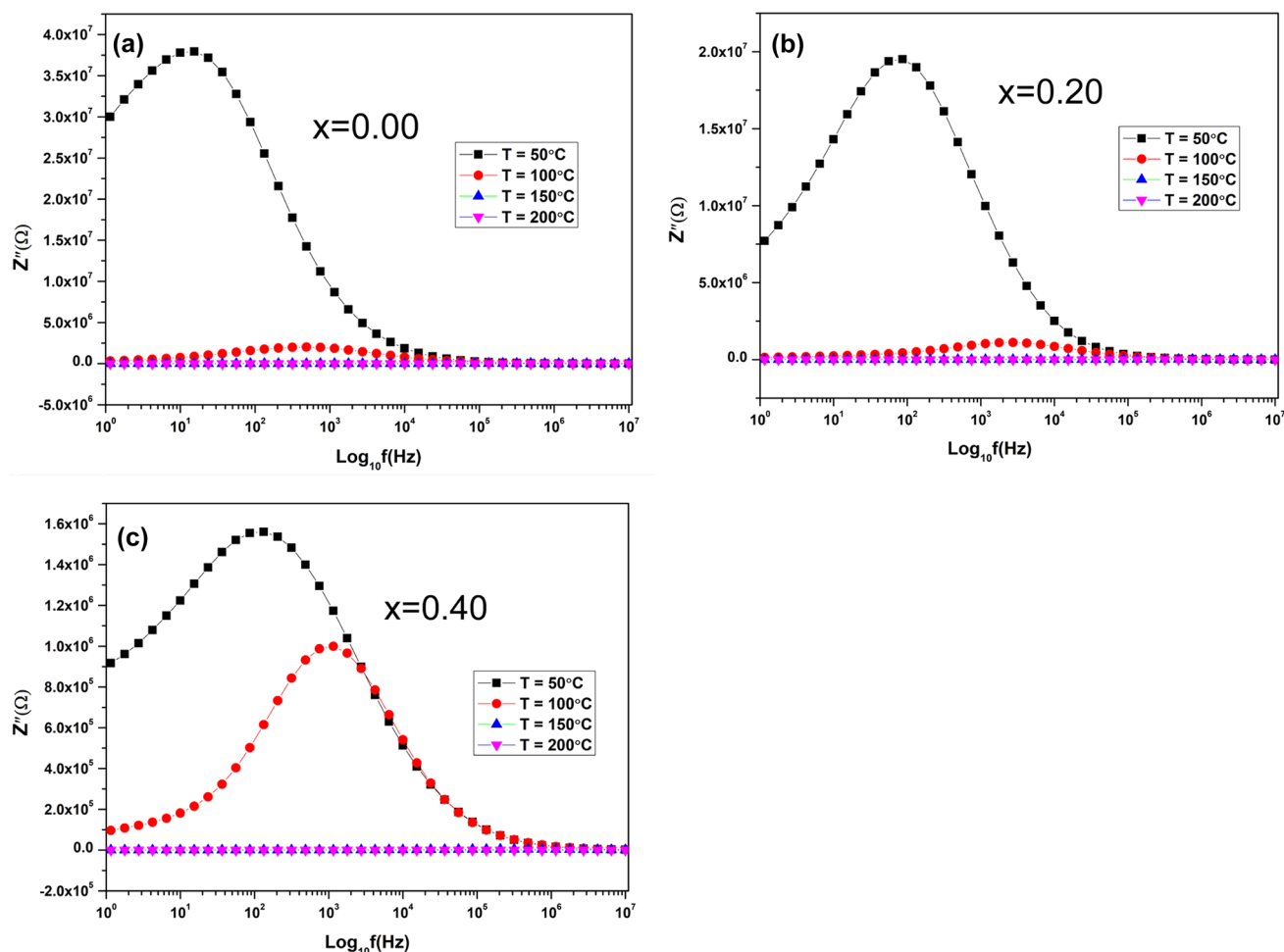


Fig. 10 Variation of Z'' against frequency with varying temperatures for $\text{Ni}_{1-x}\text{Mg}_x\text{Fe}_2\text{O}_4$: (a) 0.00, (b) 0.20 and (c) 0.40.

With increasing temperature, the Nyquist curve almost becomes minimal or resistance becomes almost negligible. The change in the intercept of the Cole–Cole plot with the subsequent rise in temperature confirms the occurrence of the non-Debye relaxation process in the Mg-doped nickel ferrites.³¹ This effect is basically due to the presence of oxygen vacancies and defects present in the crystal lattice. The decreasing ionic radii with the increasing temperatures exhibit the negative temperature coefficient of the resistance characteristic present in the ferrite.

Fitting of Nyquist Plots

The fitting of the Nyquist's plots has been carried out to calculate the values of the grain, grain boundary resistance, and constant phase element using ESimp Win software, as shown in Fig. 12a, b, and c. Series of a parallel RC circuit containing separate grains and grain boundaries as shown in Fig. 12d. The fitted values of the grain and grain boundary resistances and capacitances are set out in Table V. High

values of grain boundary resistance signifies the production of defects trapping the conducting charges.³² The contribution of the grain capacitance, C_g , was in the nF range and the R_g varies in the KΩ range contributed to the least defective structure obtained upon the doping of the magnesium.

AC Conductivity

The plots of AC conductivity against frequency have been obtained at room temperature for all the prepared compositions of Mg-doped nickel ferrites ($\text{Ni}_{1-x}\text{Mg}_x\text{Fe}_2\text{O}_4$, $x = 0.00, 0.20$ and 0.40), as shown in Fig. 13a, b, and c. The Jonscher power law fitting has also been carried out for all the plots to obtain the values of P_1 (DC conductivity), P_2 (A), and P_3 (s), as shown in Table VI.

The Jonscher power law fitting equation is:

$$\sigma(\omega) = \sigma_{DC} + A\omega^s \quad (10)$$

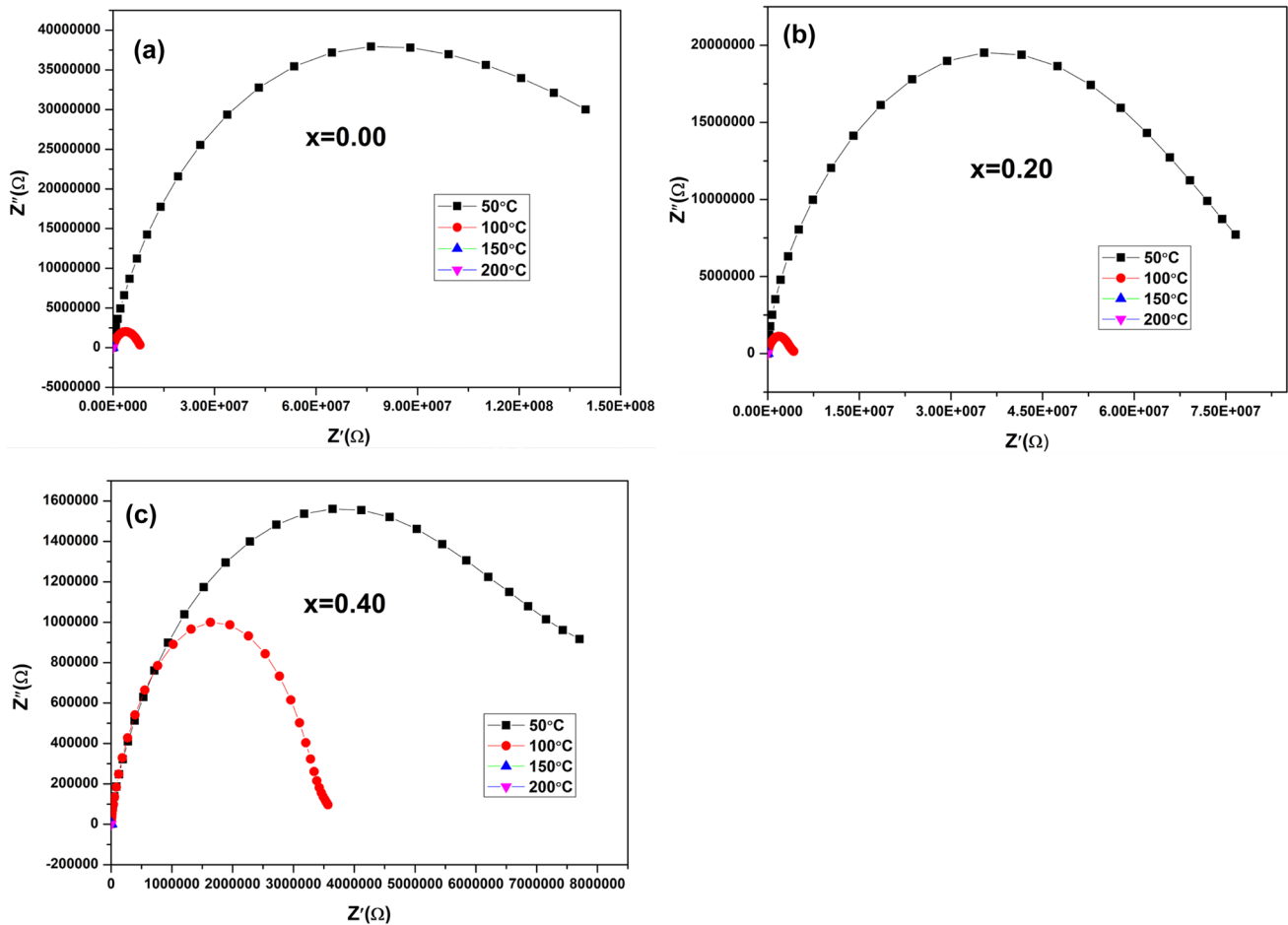


Fig. 11 Nyquist plots for the $\text{Ni}_{1-x}\text{Mg}_x\text{Fe}_2\text{O}_4$ ferrites: (a) 0.00, (b) 0.20, and (c) 0.40 at different temperatures.

where σ_{DC} represents DC conductivity, A is a constant, ω represents the frequency given by $2\pi f$ (f denoted the applied frequency), and s is the power exponent.

AC conductivity plots show linear behavior with frequency which is in good agreement with the normal behavior of dielectrics. It has been observed that, with increasing the concentration of magnesium ions, the value of DC conductivity has also been increased, from $6.425\text{E}-09$ to $3.03\text{E}-08$. This increase in the conductivity values mainly occurs due to the rise in the rate of the hopping mechanism of Fe^{2+} and Fe^{3+} ions.³² The hopping of charge carriers between Fe atoms is n -type, while p -type hopping has occurred on adding the Mg ions in the nickel ferrite. This p -type hopping has been taking place due to the Mg doping between the two charged states of Mg^+ and Mg^{2+} , and hence contributes towards the increase in conductivity of the samples with increasing magnesium ion concentration.³³

Plot of DC Conductivity with Temperature

The variation of DC conductivity with temperature for Mg-substituted nickel ferrites is shown in Fig. 14 obtained at room temperature. The activation energy for pure nickel ferrite is 1.14 eV corresponding to the motion of oxygen vacancies, while for Mg-substituted nickel ferrites (20% and 40%), the activation energy values have been reduced from 1.08 to 1.068 eV. The existence of oxygen vacancies is due to the mixing of ions ($\text{Fe}^{2+}/\text{Fe}^{3+}$) during the sintering process.³⁴ The activation energy for 40% Mg-doped nickel ferrite is the lowest around 1.06 eV, which is associated with the increased hopping conduction mechanism.

VSM Analysis

The magnetic properties of the Mg-doped nickel ferrite nanoparticles ($\text{Ni}_{1-x}\text{Mg}_x\text{Fe}_2\text{O}_4$, $x = 0.00, 0.20$ and 0.40) have been analyzed with the help of VSM. Figure 15 shows the variation of magnetization (M) against the applied magnetic field (H) of 1 T (-1 KOe to $+1$ KOe). The values

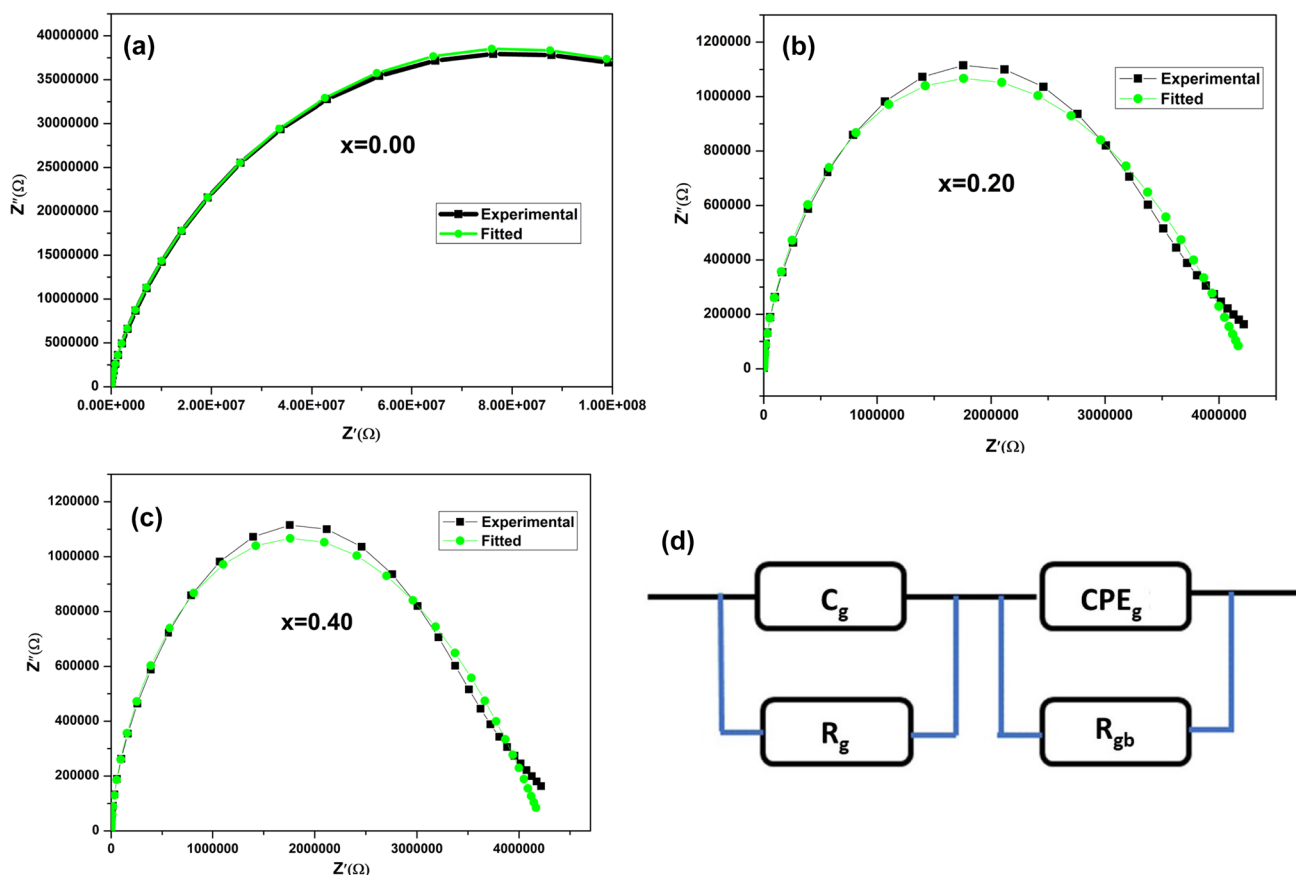


Fig. 12 Fitted Nyquist plots for the $\text{Ni}_{1-x}\text{Mg}_x\text{Fe}_2\text{O}_4$ ferrites: (a) $x = 0.00$, (b) $x = 0.20$, (c) $x = 0.40$, and (d) equivalent circuit diagram.

Table V Fitted parameters (R_g , R_{gb} , C_g and CPE_g) obtained for Mg-doped nickel ferrite nanoparticles, $\text{Ni}_{1-x}\text{Mg}_x\text{Fe}_2\text{O}_4$ ferrite ($x = 0.00, 0.20, \text{ and } 0.4$)

Composition	R_g (Ω)	C_g (F)	R_{gb} (Ω)	CPE_g (F)
$x = 0.00$	3.2×10^4	10.5×10^{-9}	9100000	6.5×10^{-9}
$x = 0.20$	0.85×10^4	5.50×10^{-9}	7300000	3.91×10^{-8}
$x = 0.40$	0.70×10^4	2.78×10^{-9}	4780000	2.81×10^{-7}

of coercive field (H_c), remanent magnetization (M_r), saturation magnetization (M_s), and squareness ratio are shown in Table VII. The results exhibit a decrease in the H_c and M_s values with the increase in the concentration of Mg^{2+} ions. The smaller values of H_c and M_r contribute towards the superparamagnetic behavior in the prepared composition.³⁵ It has been shown that most of the magnetic nanoparticles exhibit much lower values of M_s compared to the bulk form.³⁶

The reduction in magnetic properties is related to the cationic distribution of ions among the A as well as the B sites. In a ferromagnetic spinel ferrite, magnetization mainly arises due to the superexchange interaction between metal

ions present at the octahedral (B) and tetrahedral (A) sites. This mainly gets attributed due to the migration of Fe^{3+} ions from the A to the B sites with rising Mg content. This migration of ions will lead to more Fe^{3+} content at the B sites which initiates a spin-canting phenomenon, resulting in the weakening of the A–B interaction. Hence, it will lead to a reduction in the saturation magnetization from 27.90 to 16.39 emu/g.³⁷ According to Neel’s theory of ferrimagnetism, there are three main types of interaction occurring between unpaired electrons of cations located at the A and B lattice sites. They are called, A–A interaction, A–B interaction, and B–B interaction. Among them, A–B interactions are the strongest. The exchange interaction between the A and B sites is the main reason behind the variation in the magnetic properties of spinel ferrites

$$\text{Squareness ratio} = \frac{M_r}{M_s} \tag{11}$$

Stoner and Wohlfarth have reported that, if this ratio is less than 0.5, then it indicates that the interaction between particles take place only through magnetostatic interactions. The formula for calculating the squareness ratio is given by Eq. (11). If this

ratio is greater than 0.5, then it means there are randomly ori-

recent reported literature,³⁹ including the fact that the values

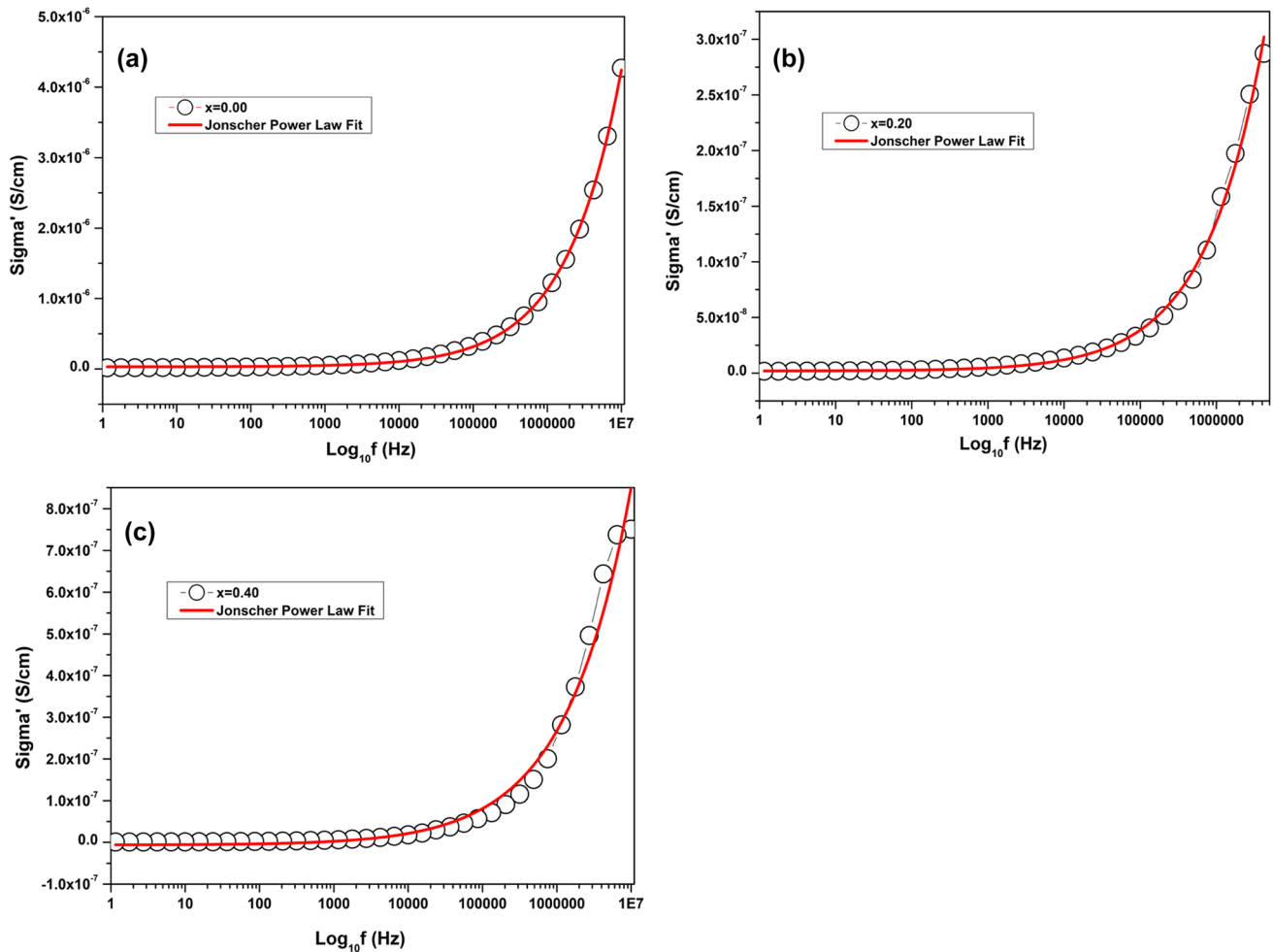


Fig. 13 Variation of AC conductivity against frequency for $\text{Ni}_{1-x}\text{Mg}_x\text{Fe}_2\text{O}_4$ ferrites: (a) 0.00, (b) 0.20, and (c) 0.40 obtained at room temperature.

Table VI Enlisted values of DC conductivity, A , and s (exp factor) for Mg^{2+} -doped nickel ferrites, $\text{Ni}_{1-x}\text{Mg}_x\text{Fe}_2\text{O}_4$

Composition	P_1 (σ_{dc})	P_2 (A)	P_3 (S)	E_g (eV)
$X = 0.00$	3.03799E-08	1.18391E-10	0.58364	1.14
$X = 0.20$	1.87724E-9	1.26856E-11	0.56093	1.08
$X = 0.40$	6.481825E-09	1.17322E-10	0.49549	1.07

ented particles that undergo rotation under an applied magnetic field.³⁸ All the prepared samples have their squareness ratio in the range of 0.2–0.3 or less than 0.5, which means that they all possess interactions taking place only as magnetostatic interactions.

The measurement of superparamagnetic behavior is justified by calculating the squareness ratio (SQR). The values of SQR have been found to be in good agreement with the

of saturation magnetization and coercivity are both decreasing with the rise in the doping% of Mg^{2+} ion in the nickel ferrites. The superparamagnetic behavior is more prominent for the samples having SQR values as small as possible. If the value of the SQR or the ratio of $M_r/M_s < 0.5$, then the prepared samples are very less anisotropic and contain more pronounced spin-canting effects, which lead to the production of more superparamagnetic nanoparticles.⁴⁰

Conclusions

Mg -doped nickel ferrite nanoparticles ($\text{Ni}_{1-x}\text{Mg}_x\text{Fe}_2\text{O}_4$; $0 \leq x \leq 0.40$) were prepared using a sol-gel auto-combustion route and correspondingly, the changes in the structural, electrical, and magnetic properties of pure nickel ferrites on adding Mg^{2+} ions have been studied. The XRD analysis revealed the

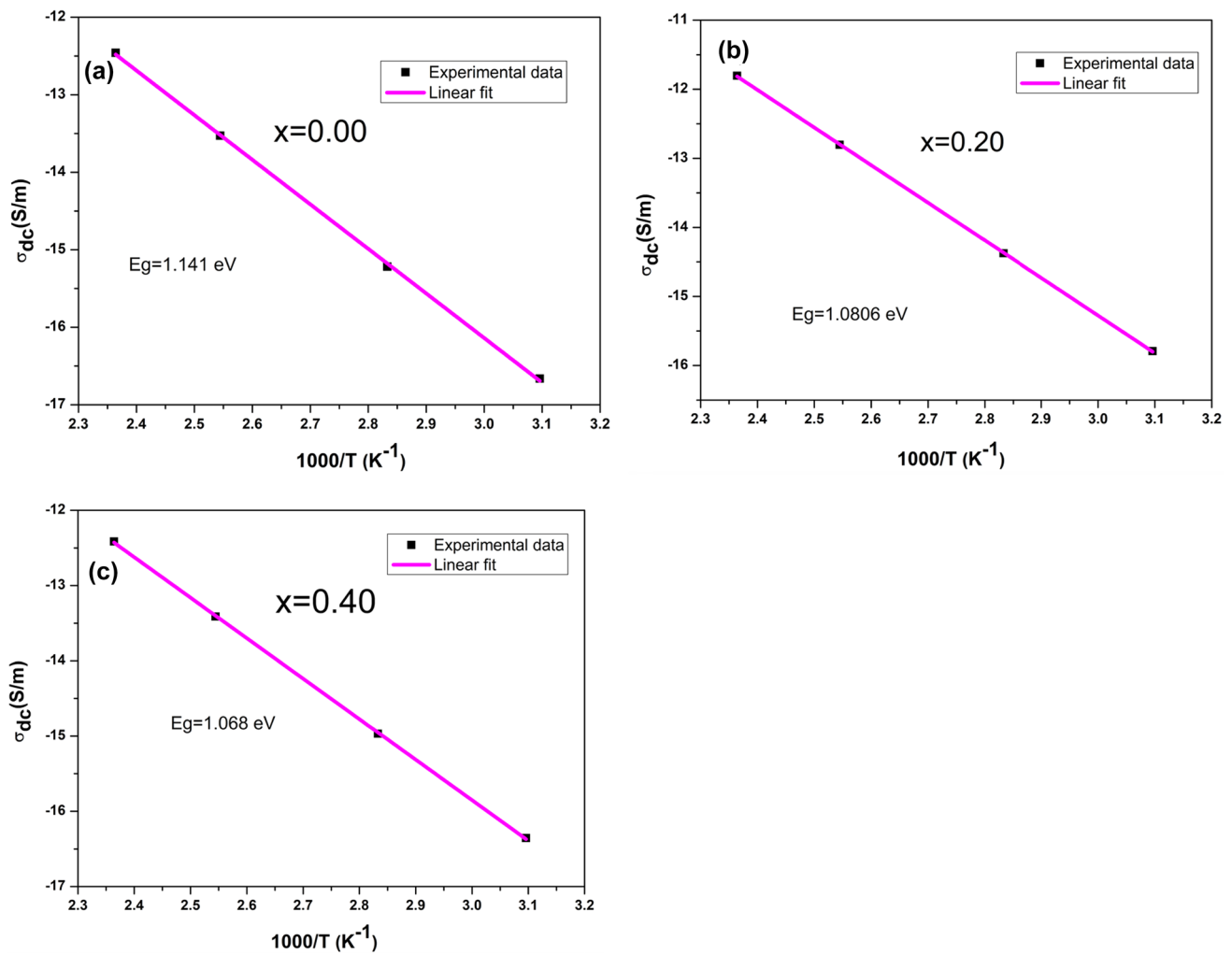


Fig. 14 Variation of DC conductivity against $1000/T$ for $Ni_{1-x}Mg_xFe_2O_4$ ferrites: (a) 0.00, (b) 0.20, and (c) 0.40 obtained at room temperature.

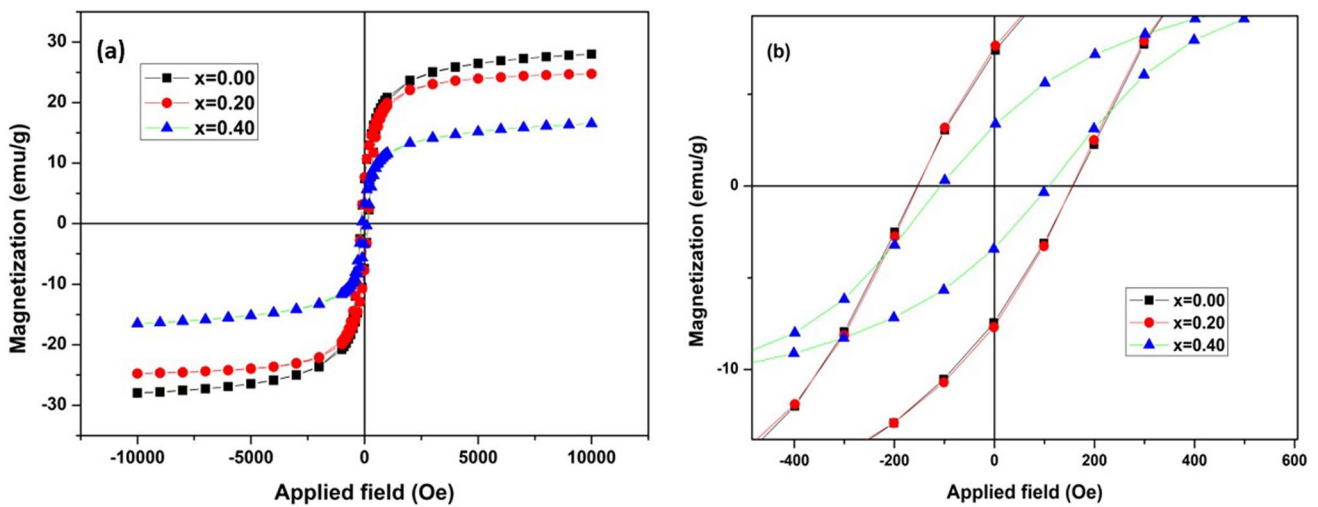


Fig. 15 Magnetic hysteresis loops for Mg-doped nickel ferrites, $Ni_{1-x}Mg_xFe_2O_4$: (a) 0.00, 0.20, and 0.40, (b) enlarged view of M-H loop of the samples at room temperature.

Table VII Values of M_r , M_s , and H_c for the Mg-doped nickel ferrites nanoparticles under the applied field of 1 T obtained at room temperature

Composition	Saturation magnetization (M_s) (emu/g)	Remanent magnetization (M_r) (emu/g)	Coercive field (H_c) (Oe)	Squareness ratio
$X = 0.00$	27.744	7.085	155.03	0.2555
$X = 0.20$	24.932	7.763	155.01	0.3113
$X = 0.40$	16.752	3.421	109.57	0.2042

cubic structure of the prepared spinel ferrites with the crystallite size varying between 27 and 36 nm. The particle size of the prepared nanoparticles has been found to be in the range of 37–69 nm. A single phase cubic structure has been confirmed from the FTIR absorption bands observed around 400 cm^{-1} and 547 cm^{-1} , which correspond to the vibrations due to the tetrahedral and octahedral sites. Dielectric studies revealed the presence of Maxwell–Wagner polarization. AC conductivity increases with the increase in the frequency due to the hopping of charge carriers. Magnetization has been reduced from 27.744 to 16.752 emu/g with the doping of magnesium with the successive reduction in the coercivity. The radii of the semicircles obtained in the Cole–Cole plots also reduce with the subsequent rise in temperature, indicating the increase in the hopping mechanism of the Fe^{3+} ions. Smaller values of coercivity lead to the soft magnetic behavior of the prepared nanoparticles, which have shown low dielectric losses in the high-frequency range and hence can be preferred for high-frequency device applications.

Conflict of interest The Authors declare no competing interests.

References

- M.K. Shobana, K. Kim, and J.H. Kim, Impact of magnesium substitution in nickel ferrite: optical and electrochemical studies. *Phys. E* 108, 100 (2019)
- P. Chavan, L.R. Naik, P.B. Belavi, G. Chavan, C.K. Ramesha, and R.K. Kotnala, Studies on electrical and magnetic properties of Mg-substituted nickel ferrites. *J. Electron. Mater.* 46, 188 (2017)
- D.R.S. Gangaswamy, M.C. Varma, S. Bharadwaj, K. Sambasiva Rao, and K.H. Rao, Comparison study of structural and magnetic properties of magnesium-substituted nickel-zinc ferrites synthesized by solid-state and sol–gel routes. *J. Supercond. Novel Magn.* 28, 3599 (2015)
- B.P. Jacob, A. Kumar, R.P. Pant, S. Singh, and E.M. Mohammed, Influence of preparation method on structural and magnetic properties of nickel ferrite nanoparticles. *Bull. Mater. Sci.* 34, 1345 (2011)
- M. Naeem, N.A. Shah, I.H. Gul, and A. Maqsood, Structural, electrical and magnetic characterization of Ni-Mg spinel ferrites. *J. Alloy. Compd.* 487(1–2), 739 (2009)
- M.A. Dar, V. Verma, S.P. Gairola, W.A. Siddiqui, R.K. Singh, and R.K. Kotnala, Low dielectric loss of Mg doped Ni-Cu-Zn nano-ferrites for power applications. *Appl. Surf. Sci.* 258(14), 5342 (2012)
- A. Nadumane, K. Shetty, K.S. Anantharaju, H.P. Nagaswarupa, D. Rangappa, Y.S. Vidya, and S.C. Prashantha, Sunlight photocatalytic performance of Mg-doped nickel ferrite synthesized by a green sol-gel route. *J. Sci.: Adv. Mater. Devices* 4(1), 89 (2019)
- A. Sattar, B. Bofeng, M. Khalil, and M. Sajjad, Detailed analysis of structural, optical and photo catalytic properties of spinel nickel doped magnesium zinc ferrites at different substitutions. *Inorg. Chem. Commun.* 142, 109505 (2022)
- R. Arulmurugan, G. Vaidyanathan, S. Sendhilnathan, and B. Jeyadevan, Thermomagnetic properties of $\text{Co}_{1-x}\text{Zn}_x\text{Fe}_2\text{O}_4$ ($x = 0.1\text{--}0.5$) nanoparticles. *J. Magn. Magn. Mater.* 303(1), 131 (2006)
- H.S. Mund and B.L. Ahuja, Structural and magnetic properties of Mg doped cobalt ferrite nano particles prepared by sol-gel method. *Mater. Res. Bull.* 85, 228 (2017)
- J.M. Gao, M. Zhang, and M. Guo, Innovative methodology for comprehensive utilization of saprolite laterite ore: recovery of metal-doped nickel ferrite and magnesium hydroxide. *Hydrometallurgy* 158, 27 (2015)
- M.P. Reddy, R.A. Shakoor, A.M.A. Mohamed, M. Gupta, and Q. Huang, Effect of sintering temperature on the structural and magnetic properties of MgFe_2O_4 ceramics prepared by spark plasma sintering. *Ceram. Int.* 42(3), 4221 (2016)
- H. Moradmard, S.F. Shayesteh, P. Tohidi, Z. Abbas, and M. Khaleghi, Structural, magnetic and dielectric properties of magnesium doped nickel ferrite nanoparticles. *J. Alloy. Compd.* 650, 116 (2015)
- M. Mostafa, O. Saleh, A.M. Henaish, S.A. Abd El-Kaream, R. Ghazy, O.M. Hemeda, and M.A. Darwish, Structure, morphology and electrical/magnetic properties of Ni-Mg nano-ferrites from a new perspective. *Nanomaterials* 12(7), 1045 (2022)
- D. Ravinder, M. Hashim, A. Upadhyay, M.M. Ismail, S. Kumar, R. Kumar, and A. Khalilullah, Investigation of structural and magnetic properties of La doped Co-Mn ferrite nanoparticles in the presence of $\alpha\text{-Fe}_2\text{O}_3$ phase. *Solid State Commun.* 342, 114629 (2022)
- A. Sutka, S. Lagzdina, G. Mezinskis, A. Pludons, I. Vitina, and L. Timma, A comparative study of $\text{Ni}_{0.7}\text{Zn}_{0.3}\text{Fe}_2\text{O}_4$ obtained by sol-gel auto-combustion and flash combustion methods. In IOP Conference Series: Materials Science and Engineering (Vol. 25, No. 1, p. 012019). IOP Publishing. (2011)
- R. Tholkappian and K. Vishista, Combustion synthesis of Mg-Er ferrite nanoparticles: cation distribution and structural, optical, and magnetic properties. *Mater. Sci. Semicond. Process.* 40, 631 (2015)
- P.B. Kharat, S.D. More, S.B. Somvanshi, and K.M. Jadhav, Exploration of thermoacoustics behavior of water based nickel ferrite nanofluids by ultrasonic velocity method. *J. Mater. Sci. Mater. Electron.* 30, 6564 (2019)
- S.V. Bhandare, R. Kumar, A.V. Anupama, M. Mishra, R.V. Kumar, V.M. Jali, and B. Sahoo, Effect of Mg-substitution in Co-Ni-Ferrites: cation distribution and magnetic properties. *Mater. Chem. Phys.* 251, 123081 (2020)
- P.A. Udhaya, T.C. Bessy, and M. Meena, Antibacterial activity of nickel and magnesium substituted ferrite nanoparticles synthesized via self-combustion method. *Mater Today Proc.* 8, 169 (2019)
- N. Kavitha and P. Manohar, Magnetic and electrical properties of magnesium-substituted Ni-Zn ferrites. *J. Supercond. Novel Magn.* 29, 2151 (2016)
- S. Kumar, P.B. Barman, and R.R. Singh, Estimation and association of structural, elastic and magnetic properties of magnesium-nickel-ferrite nanoparticles annealed at different temperatures. *Mater. Sci. Eng. B* 272, 115362 (2021)
- K. Nadeem, M. Kamran, H.Z. Khokhar, I. Ahmed, F. Zeb, and N.A. Noshahi, Effect of Mg doping on magnetic, and dielectric

- properties of NiCr_2O_4 nanoparticles. *Ceram. Int.* 48(12), 17270 (2022)
24. M. Kumar, S. Shankar, O. Parkash, and O.P. Thakur, Dielectric and multiferroic properties of $0.75\text{BiFeO}_3\text{-}0.25\text{BaTiO}_3$ solid solution. *J. Mater. Sci. Mater. Electron.* 25, 888 (2014)
 25. S. Ali, M. Khalid, G. Nazir, K. Naz, J.K. Khan, M.S. Akhtar, and N. Abbas, Effect of nickel substitution on structural and dielectric properties of Mg-Zn based spinel ferrite nanoparticles. *Phys. Scr.* 97(6), 065802 (2022)
 26. N. Sivakumar, A. Narayanasamy, J.M. Greneche, R. Murugaraj, and Y.S. Lee, Electrical and magnetic behaviour of nanostructured MgFe_2O_4 spinel ferrite. *J. Alloy. Compd.* 504(2), 395 (2010)
 27. P. Jain, S. Shankar, and O.P. Thakur, Exploring the multiferroic and water sensing behavior of Cu/Er co-substituted ferrites as key enablers for next-gen hydroelectric cells. *Mater. Chem. Phys.* 315, 128945 (2024)
 28. P. Jain, S. Shankar, and O.P. Thakur, Unveiling the impact of Ni $2+/Y\ 3+$ co-substitution on the structural, dielectric, and impedance properties of multiferroic spinel ferrite for hydroelectric cell application. *Phys. Chem. Chem. Phys.* 25(32), 21280 (2023)
 29. M.A. Ali, M.N.I. Khan, F.U.Z. Chowdhury, S. Akhter, and M. Uddin, Structural properties, impedance spectroscopy and dielectric spin relaxation of Ni-Zn ferrite synthesized by double sintering technique. arXiv preprint [arXiv:1505.06438](https://arxiv.org/abs/1505.06438) (2015)
 30. S. Shankar, O.P. Thakur, and M. Jayasimhadri, Significant improvements in dielectric, impedance, multiferroic and magnetoelectric properties of $(1-x)\text{Co}_{0.5}\text{Ni}_{0.5}\text{Fe}_2\text{O}_4\text{-}x\text{BaTiO}_3$ bulk composites ($x=0, 0.10$ and 0.20). *J. Mater. Sci. Mater. Electron.* 32, 16706 (2021)
 31. I. Maurya, S. Shankar, O.P. Thakur, and M. Jayasimhadri, Structural and impedance spectroscopy in $\text{BiFeO}_3\text{-BiCoO}_3\text{-BaTiO}_3$ ternary system. *Mater. Today Proc.* 47, 1696 (2021)
 32. R.B. Kamble, V. Varade, K.P. Ramesh, and V. Prasad, Domain size correlated magnetic properties and electrical impedance of size dependent nickel ferrite nanoparticles. *AIP Adv.*, 5(1), (2015)
 33. G. Umapathy, G. Senguttuvan, L. John Berchmans, and V. Sivakumar, Structural, dielectric and AC conductivity studies of Zn substituted nickel ferrites prepared by combustion technique. *J. Mater. Sci. Mater. Electron.* 27, 7062 (2016)
 34. M. Kumar, S. Shankar, S. Kumar, O.P. Thakur, and A.K. Ghosh, Impedance spectroscopy and conductivity analysis of multiferroic BFO–BT solid solutions. *Phys. Lett. A* 381(4), 379 (2017)
 35. U. Ahmad, M. Afzia, F. Shah, B. Ismail, A. Rahim, and R.A. Khan, Improved magnetic and electrical properties of transition metal doped nickel spinel ferrite nanoparticles for prospective applications. *Mater. Sci. Semicond. Process.* 148, 106830 (2022)
 36. M. Hadi, K.M. Batoo, A. Chauhan, O.M. Aldossary, R. Verma, and Y. Yang, Tuning of structural, dielectric, and electronic properties of Cu doped Co-Zn ferrite nanoparticles for multilayer inductor chip applications. *Magnetochemistry* 7(4), 53 (2021)
 37. A. Verma and R. Chatterjee, Effect of zinc concentration on the structural, electrical and magnetic properties of mixed Mn-Zn and Ni-Zn ferrites synthesized by the citrate precursor technique. *J. Magn. Magn. Mater.* 306(2), 313 (2006)
 38. E.C. Stoner and E.P. Wohlfarth, A mechanism of magnetic hysteresis in heterogeneous alloys. *IEEE Trans. Magn.* 27(4), 3475 (1991)
 39. B.K. Nath, P.K. Chakrabarti, S. Das, U. Kumar, P.K. Mukhopadhyay, and D. Das, Mössbauer, x-ray diffraction and AC susceptibility studies on nanoparticles of zinc substituted magnesium ferrite. *Eur. Phys. J. B-Condens. Matter Complex Syst.* 39, 417 (2004)
 40. V.S. Sharon, V.E. Gopalan, I.A. Al-Omari, and K.A. Malini, Superparamagnetic nickel ferrite nanoparticles doped with zinc by modified sol–gel method. *J. Supercond. Novel Magn.* 35(3), 795 (2022)
- Publisher's Note** Springer Nature remains neutral with regard to jurisdictional claims in published maps and institutional affiliations.
- Springer Nature or its licensor (e.g. a society or other partner) holds exclusive rights to this article under a publishing agreement with the author(s) or other rightsholder(s); author self-archiving of the accepted manuscript version of this article is solely governed by the terms of such publishing agreement and applicable law.